









## Article

# A Symmetrical Terahertz Triple-Band Metamaterial Absorber Using a Four-Capacitance Loaded Complementary Circular Split Ring Resonator and an Ultra-Thin ZnSe Substrate

Yadgar I. Abdulkarim <sup>1,2</sup>, Fatih Özkan Alkurt <sup>3</sup>, Halgurd N. Awl <sup>4</sup>, Olcay Altıntaş <sup>3</sup>, Fahmi F. Muhammadsharif <sup>5</sup>, Bhargav Appasani <sup>6,\*</sup>, Mehmet Bakır <sup>7</sup>, Muharrem Karaaslan <sup>3</sup>, Mohamed Taouzari <sup>8</sup> and Jian Dong <sup>1</sup>

- <sup>1</sup> School of Computer Science and Engineering, Central South University, Changsha 410075, China; Yadgar.kharkov@gmail.com (Y.I.A.); dongjian@csu.edu.cn (J.D.)
  - <sup>2</sup> Medical Physics Department, College of Medicals & Applied Science, Charo University, Sulaimania 46001, Iraq
  - <sup>3</sup> Department of Electrical-Electronics Engineering, Iskenderun Technical University, Hatay 31200, Turkey; fozkan.alkurt@iste.edu.tr (F.Ö.A.); olcayaltintas@gmail.com (O.A.); muharrem.karaaslan@iste.edu.tr (M.K.)
  - <sup>4</sup> Department of Communication Engineering, Sulaimani Polytechnic University, Sulaimani 46001, Iraq; halgurd.awl@spu.edu.iq
  - <sup>5</sup> Department of Physics, Faculty of Science and Health, Koya University, Koya 44023, Iraq; fahmi.fariq@koyauniversity.org
  - <sup>6</sup> School of Electronics Engineering, KIIT University, Bhubaneswar 751024, Odisha, India
  - <sup>7</sup> Department of Computer Engineering, Bozok University, Yozgat 66200, Turkey; mehmet.bak@gmail.com
  - <sup>8</sup> Laboratory LISA, National School of Applied Sciences, Hassan 1st University, Berrechid 26100, Morocco; mohamed.taouzari@uhp.ac.ma
- \* Correspondence: bhargav.appaasanifet@kiit.ac.in



**Citation:** Abdulkarim, Y.I.; Özkan Alkurt, F.; Awl, H.N.; Altıntaş, O.; Muhammadsharif, F.F.; Appasani, B.; Bakır, M.; Karaaslan, M.; Taouzari, M.; Dong, J. A Symmetrical Terahertz Triple-Band Metamaterial Absorber Using a Four-Capacitance Loaded Complementary Circular Split Ring Resonator and an Ultra-Thin ZnSe Substrate. *Symmetry* **2022**, *14*, 1477. <https://doi.org/10.3390/sym14071477>

Academic Editors: Sergei D. Odintsov, Giuseppe Iastaldi, Ben-Xin Wang, Han Xiong and Qi Lin

Received: 19 June 2022

Accepted: 13 July 2022

Published: 19 July 2022

**Publisher's Note:** MDPI stays neutral with regard to jurisdictional claims in published maps and institutional affiliations.



**Copyright:** © 2022 by the authors. Licensee MDPI, Basel, Switzerland. This article is an open access article distributed under the terms and conditions of the Creative Commons Attribution (CC BY) license (<https://creativecommons.org/licenses/by/4.0/>).

**Abstract:** In this research work, a symmetrical four-capacitance loaded complementary circular split ring resonator is proposed, which uses an ultra-thin Zinc Selenide (ZnSe) substrate to realize a low-profile triple-band metamaterial (MTM) perfect absorber for application in the terahertz (THz) frequency range. The electromagnetic properties of the proposed structure were calculated and investigated using the Finite Integration Technique (FIT). The proposed structure exhibited three highly absorptive (nearly perfect) peaks at the resonance frequencies of 15.68 THz, 37.48 THz, and 39.55 THz. Furthermore, the absorber was found to be insensitive to the polarization and incident wave angles, due to its symmetrical design. The effects of the conductor type, substrate thickness, unit cell dimension, resonator gap, and substrate type on the reflection and absorption spectra were investigated. To validate the numerical results, the proposed design was analyzed using High-Frequency Simulation Software (HFSS) and Advanced Design System (ADS). The surface current, electric field, and magnetic field distributions at the three-resonance frequency were analyzed. It was concluded that the overall performance of the proposed MTM structure was superior compared to those reported in the literature. The proposed design could be a good candidate for application in stealth technology, imaging, and thermal energy harvesting.

**Keywords:** metamaterial (MTM); complementary circular split ring resonator (CCSRR); triple-band; polarization independent; ultra-thin layer; symmetry

## 1. Introduction

Metamaterials (MTMs) are artificial structures that exhibit exotic properties of negative permittivity, negative permeability, and a negative refractive index in the frequency range of interest [1]. Metamaterials can be used for various applications such as sensing [2,3], super lensing [4,5], cloaking [6,7], imaging [8], antennae [9], and wave absorption [10]. Studies on micro- and nano-sized designs in high frequency bands have been paired with

technological developments; this is specifically important for the development of high chemical selectivity and the penetration of opaque materials. Along this line, a high-performance metamaterial-based swastika-shaped liquid chemical sensor was designed for X band applications [11]. It is known that selective designs are necessary for the production of effective electromagnetic wave absorbers that can be used in sensing, imaging, and detection applications. Therefore, various design structures have been proposed to act as a perfect absorber for the MTM resonators [12–16].

For instance, a real-time and non-invasive glucose-sensing structure, based on MTM transmission line theory, was designed and experimentally investigated in microwave frequencies [17]. Furthermore, it is possible to detect liquid chemicals such as clean and waste transformer oil, cotton oil, corn oil, and olive oil with the help of metamaterial-based sensors integrated into the X-band waveguide [18]. Recently, Chen et al., proposed an InSb micro cylinder array with a metasurface absorber for sensing applications in chemical, biological, and optoelectronic samples in the terahertz frequency range [19]. The detection rate can be correlated with effective changes in the materials' permittivity [20]. In addition, the temperature-sensing capability of metamaterial-based sensors has attracted attention in the terahertz frequencies [21–23]. The polarization-independent frequency selective thermal emitter has also been presented in the literature, revealing a relatively high sensing capability [24,25].

Terahertz absorbers are also used for the control of thermal emissions [26]. Ito et al. presented a phase change material with a metasurface to invert the thermal radiative contrast, which can control the radiative heat flux [27]. For this purpose, Zhang et al. designed a metamaterial-based optical absorber that uses the parity symmetric fano resonance principle to control the thermal resonance [28]. Additionally, metamaterial-based absorber structures have successfully been used in solar cell applications to provide high efficiency and dual-band absorption [29,30] or wideband characteristics [31]. The ability of thermal radiation has to be further explored due to its high bandwidth characteristics. Li and Fan reviewed the recent developments in the nanophotonic control of thermal radiation, photovoltaic systems, and energy harvesting [32]. Wang et al., designed a self-adaptive radiative cooling and heating system based on a solar metasurface structure [33]. In terahertz absorber structures, the achievement of a perfect wideband absorption of the light wave is possible with epsilon zero metamaterial resonators [34]. Additionally, the tunability properties of metamaterial absorbers can be obtained by amalgamating various resonators such as graphene [35,36] and strontium titanate in the terahertz bands [37]. The main purpose of adjusting the operating frequency is to control the design parameters of the resonators in either the microwave or terahertz frequencies [38–49]. Zinc selenide (ZnSe) is an attractive wide bandgap semiconductor mostly used in infrared components, windows, and lenses. ZnSe nanoparticles have been utilized in humidity sensing [50]. The interesting characteristics of zinc selenide (ZnSe) include its low electrical resistivity, high direct band gap, high refractive index, transparency over a wide frequency range, low optical absorption, and great photosensitivity. Researchers frequently employ ZnSe for applications in solar cells, sensing, and mid-infrared sources because of these characteristics [51–53]. Two-dimensional ZnSe nano sheets have recently been synthesized and systematically analyzed for wideband absorption applications [51]. An MTM-based design has also been proposed by Cheng et al. for wide-angle terahertz wave absorption, polarization-insensitive, and switchable metamaterial absorbers [54]. Various MTM designs and approaches have been reported in the literature that can be adapted to absorb incident electromagnetic waves [55]. However, most of these designs are found to be complex and expensive. Hence, researchers aim to achieve simple and cost-effective designs for MTMs, with affordable efficiency in the desired frequency ranges.

Therefore, in this work, an attempt was made to present a simple design for MTMs based on ultra-thin ZnSe to produce a triple-band metamaterial perfect absorber. The proposed design was realized by loading four capacitances in the circular split-ring resonators with a complementary scheme that can be viably used for terahertz applications.

The results showed three intensive peaks at the resonance frequencies of 15.68, 37.48, and 39.55 THz, with corresponding peak absorptions of 99%, 99.85%, and 92.25%, respectively. The overall performance of the proposed structure outperformed those reported in the literature. The novelties of the proposed structure are a low-profile and simple design that provides perfect absorption responses with independent-polarization angles in the mid-IR region and large frequency bands. The recommended metamaterials can be effectively used in thermal energy harvesting, stealth technology, and imaging applications.

## 2. Proposed Structure of the MTM Unit Cell

The proposed triple-band perfect metamaterial absorber structure is shown in Figure 1, while the optimum parameters of the proposed design are given in Table 1. As can be seen in the periodic array shown in Figure 1a–c, the top ( $h_3$ ) and bottom ( $h_1$ ) layers were composed of copper, while the middle layer ( $h_2$ ) was made of ZnSe.  $\Delta w$ ,  $l$ ,  $g$ ,  $R$ ,  $r$ , and  $D$  were the resonator's dimensions.  $L$  and  $W$  were the length and width of the proposed metamaterial unit cell, respectively. The values of the conductivities of different materials were taken based on the material library of the CST software; this software is widely used for simulations of structures. In this work, the conductivity of copper was taken as  $\sigma = 5.8 \times 10^7$  S/m [56].

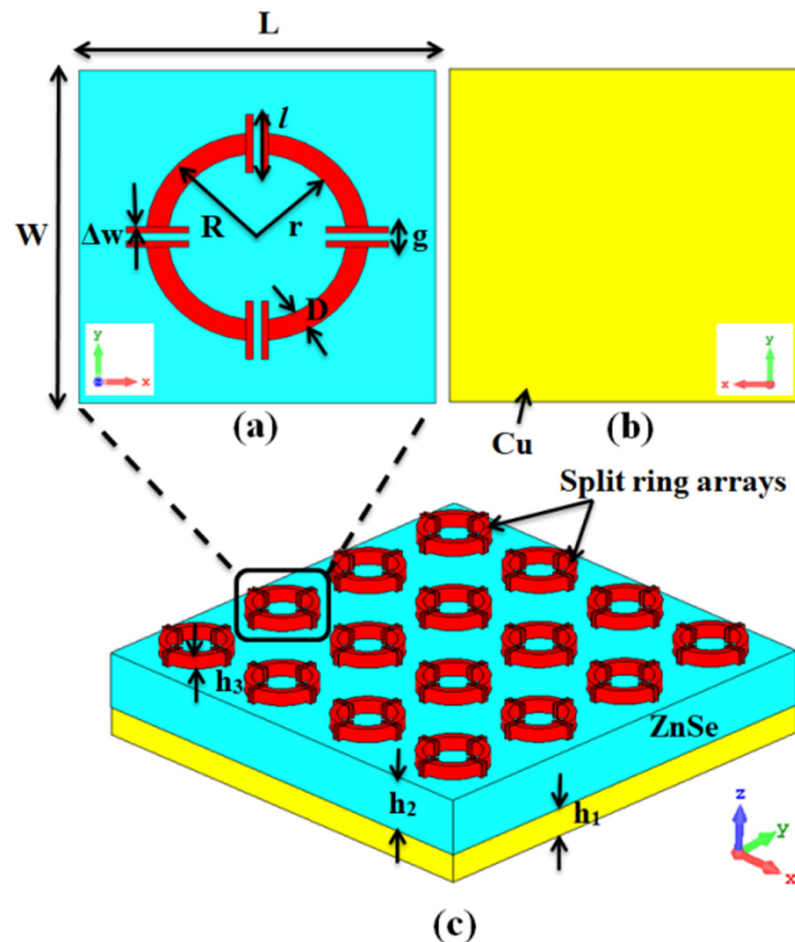


**Figure 1.** (a) Front view with dimensions, (b) bottom view, and (c) perspective view of the suggested structure.

**Table 1.** Dimensional values for the proposed MTM configuration.

Parameter	Value ( $\mu\text{m}$ )
$L$	8
$W$	8
$D$	0.5
$r$	2
$R$	2.5
$l$	1.54
$h_1$	0.03
$h_2$	0.6
$h_3$	0.03
$g$	1.8
$\Delta w$	1.15

The absorption rate can be expressed by Equation (1):

$$A(\omega) = 1 - R(\omega) - T(\omega) = 1 - |s_{11}|^2 - |s_{12}|^2 \quad (1)$$

where  $A(\omega)$ ,  $R(\omega)$ , and  $T(\omega)$  represent the absorption. The origin of the absorption can be understood from Equation (1). The structure absorbs the incident electromagnetic radiation when the transmission coefficient is zero and the reflection is zero. Zero transmission was ensured by placing a thick metallic ground that prevented the transmission of the wave; we can express the absorptivity by  $A(\omega) = 1 - |s_{11}|^2$ . The reflection coefficient has to be minimized through the proper design of the resonators on the top plane. When designed properly, the impedance of the top plane matches that of the free space, ensuring minimum reflection. For wide-band absorption, the unit parameters must be optimized to ensure that the impedance of the free space is approximately equal along this band. The proposed structure's electromagnetic properties and absorption performance were analyzed by using a Computer Simulation Technology (CST) microwave studio electromagnetic simulator, which employs the Finite Integration Technique (FIT). All the physical properties parameters of each design material were taken from the materials library of the simulation software (CST). ZnSe was added into the library of the CST software defined as a new material by providing its permittivity and permeability parameters of 5.73 and 1, respectively [52]. We set periodic boundary conditions in the x- and y- directions and applied an open-add space boundary condition in the z-direction, as shown in Figure 2b. Figure 2a exhibits the proposed structure's absorption, reflection, and transmission spectra between 13 THz and 40 THz. Perfect metamaterial absorber characteristics were observed at three peaks, namely 15.68 THz, 37.48 THz, and 39.55 THz—corresponding to absorptivities of 98.76%, 99.58%, and 92.39%, respectively. These three absorption peaks were all formed due to the electric dipole resonance. The peak occurring at 31 THz had a very low absorbance and could not be considered an absorption peak. Such peaks do not have any practical utility as they cannot absorb the incident electromagnetic radiation. Only absorption bands with a peak absorption greater than 90% are considered important.

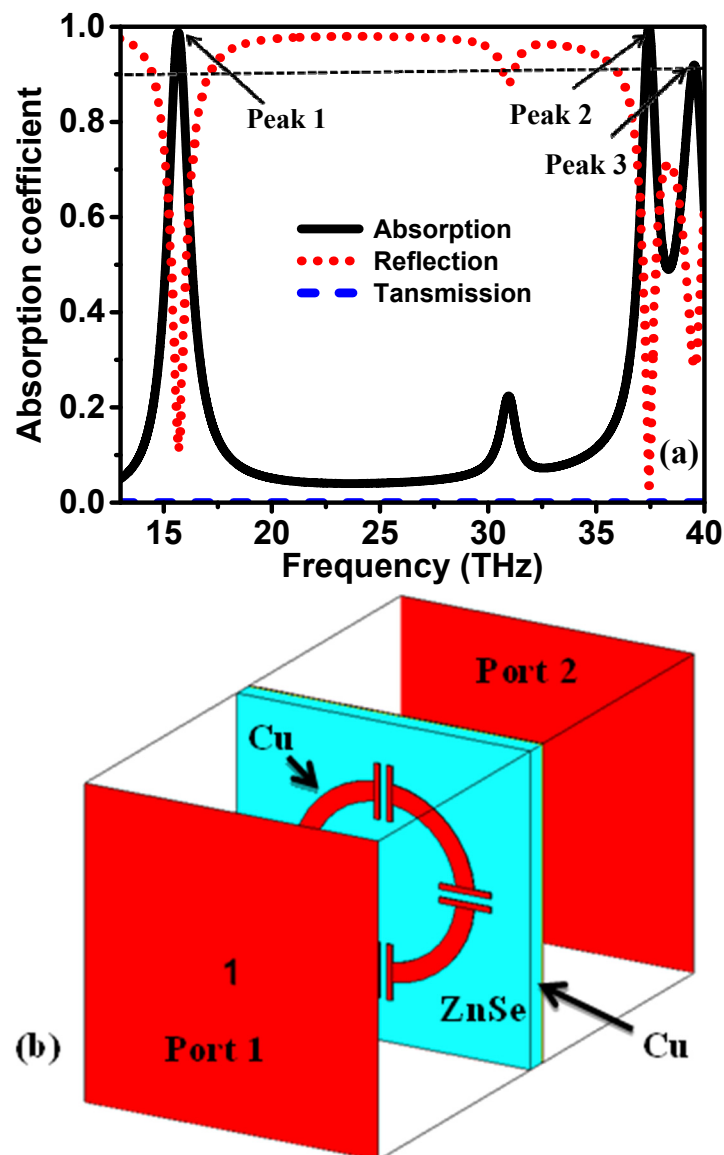


**Figure 2.** (a) Simulated reflection, absorption and transmission spectra showed resonant peak 1, peak 2, and peak 3 and (b) Boundary conditions set up with port 1 and port 2 for the designed structure.

### 3. Polarization Independence

When an electromagnetic wave is incident on an inclined metamaterial surface, the absorptivity is decreased because of the reflection of part of the wave. An ideal absorber should absorb the electromagnetic radiation independently of the angle of incidence and the polarization angle. The proposed absorber offers similar absorption characteristics for different incident angles and for different polarization angles, as shown in Figure 3. Seven different oblique incidence angles were considered between  $0^\circ$  and  $90^\circ$ , and the same absorption characteristics results were achieved. Due to the unique design of the proposed structure, the polarization and incident angle independency were obtained over the whole simulation bandwidth. A top metallic layer consisting of an array of four capacitance-loaded circle complementary metallic resonators was utilized to achieve a polarization-independent electromagnetic response. Due to the symmetrical configuration of the resonators, the changes in the optical response at different polarization angles were trivial. Generally, for a plane monochromatic electromagnetic wave in an isotropic medium, the wave vector  $k$ , magnetic field  $H$ , and electric field  $E$  are always perpendicular to each other. It can be interpreted that, in our design environment, the wave vector is in direction

of  $Z$ , which is perpendicular to the ports and structure surface. When the vectors  $E$  and  $H$  are in phase and in the directions of  $X$  and  $Y$ , respectively, they are approximately straight with respect to the rotational symmetry of the resonators along the  $X$  and  $Y$  axis. However, in some cases, novel resonators do not obey this postulate, as shown in some different works in the literature [54,56–58]. Therefore, we believe that the novelty of the proposed absorber leads to the achievement of incidence angle independence—especially for angle variations from 0 to 90 degrees.

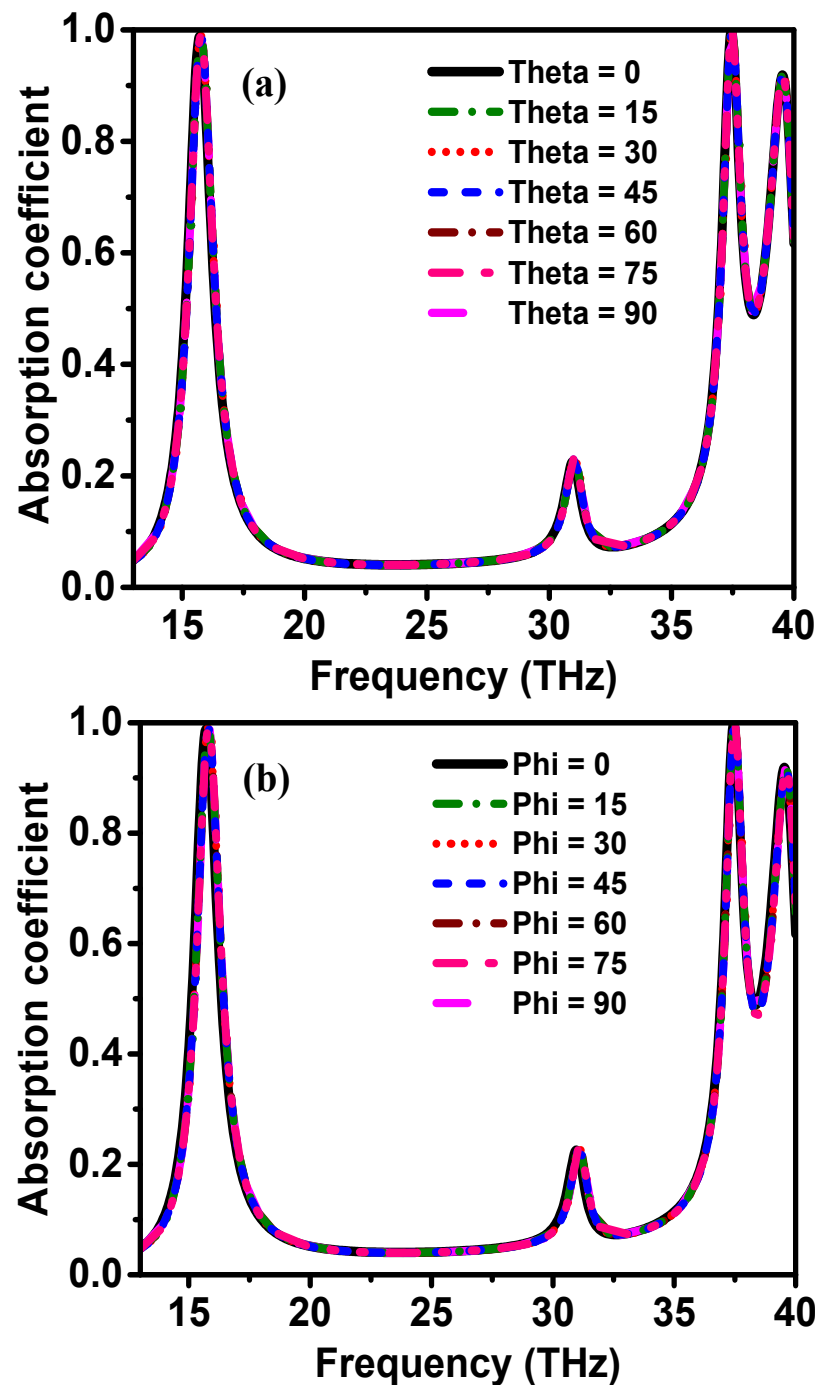


Figure 3. (a) Simulated absorption results for the suggested design at different incident angles and (b) polarization independence of the structure from  $0^\circ$  to  $90^\circ$ .

## 4. Parametric Analysis of the Reflection and Absorption Coefficient

### 4.1. Effect of Conductor Type

The metal used for the resonators significantly affects the performance of the MTM structure due to their differences in conductivity. Consequently, different conductive materials, namely Platinum, Copper, Gold, and Iron, were utilized to perform the parametric studies. The conductivity of these materials is  $9.43 \times 10^6$  S/m,  $5.80 \times 10^7$  S/m,  $4.11 \times 10^7$  S/m, and  $1 \times 10^7$  S/m, respectively, based on the material library in the CST software. Therefore, different resonance characteristics would be anticipated due to the conductivity variation of the resonator materials. Figure 4 shows the impact of changing the resonator type on the reflection and absorption spectra of the proposed MTM structure. One can notice that the positions of the resonance peaks shift with changes in the type of material. Moreover, the absorption coefficient was found to be maximal in the low and high-frequency ranges when gold was used for the metallic layers.

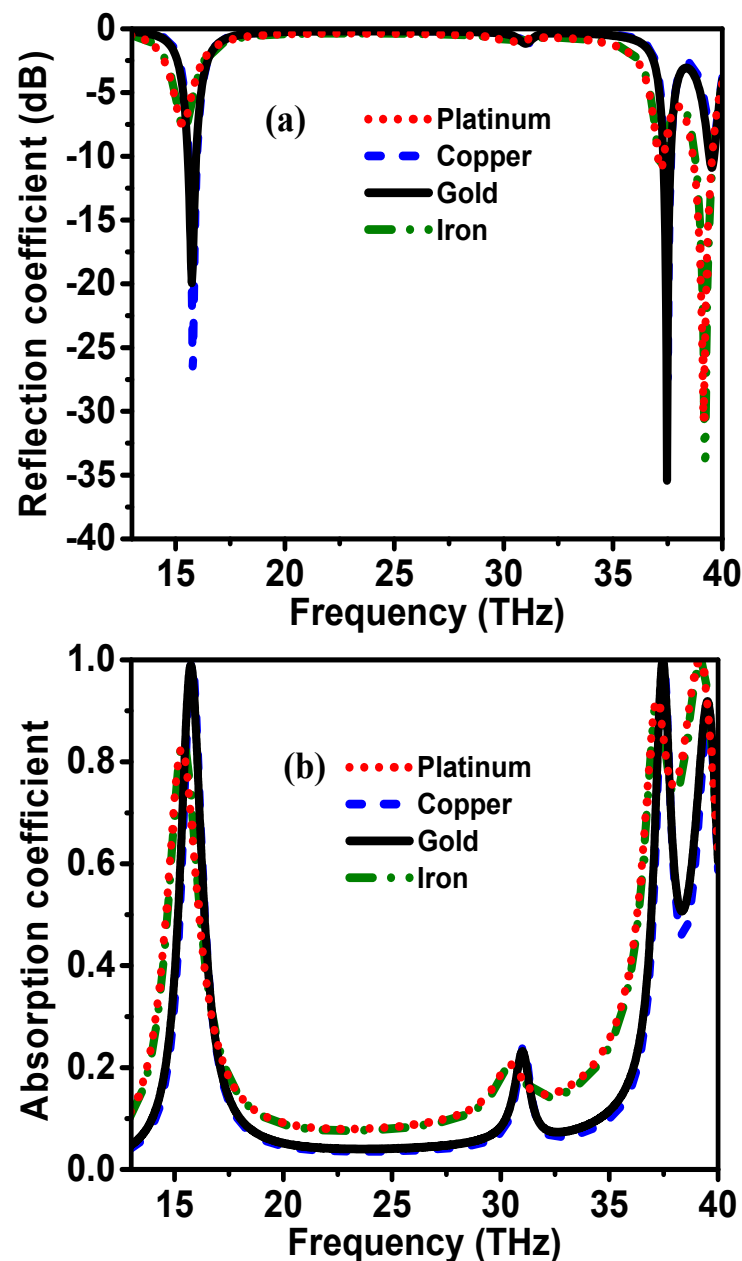


Figure 4. Effect of conductor type (resonator material) on the (a) reflection and (b) absorption coefficient of the proposed MTM.

Nevertheless, a low reflection coefficient was optimum for the MTM when iron was added as the metallic layer. These differences can be ascribed to the effect of the plasmonic resonance response of the metals on the overall absorption and reflection of the EM waves. Noticeably, platinum and iron showed nearly the same return loss and transmission characteristics because their conductivities are close to each other. Similarly, copper and gold conductors established very similar resonance characteristics due to their relative conductivity values.

#### 4.2. Effect of Substrate Thickness

The second significant parameter of the resonator design is the thickness of the dielectric substrate, as it controls the capacitive effect against the resonance frequency. As shown in Figure 5, the first resonance frequency shifted with changes in thickness and distorted the second resonance. Consequently, the optimum thickness of the ZnSe substrate layer was obtained at 0.6  $\mu\text{m}$ .

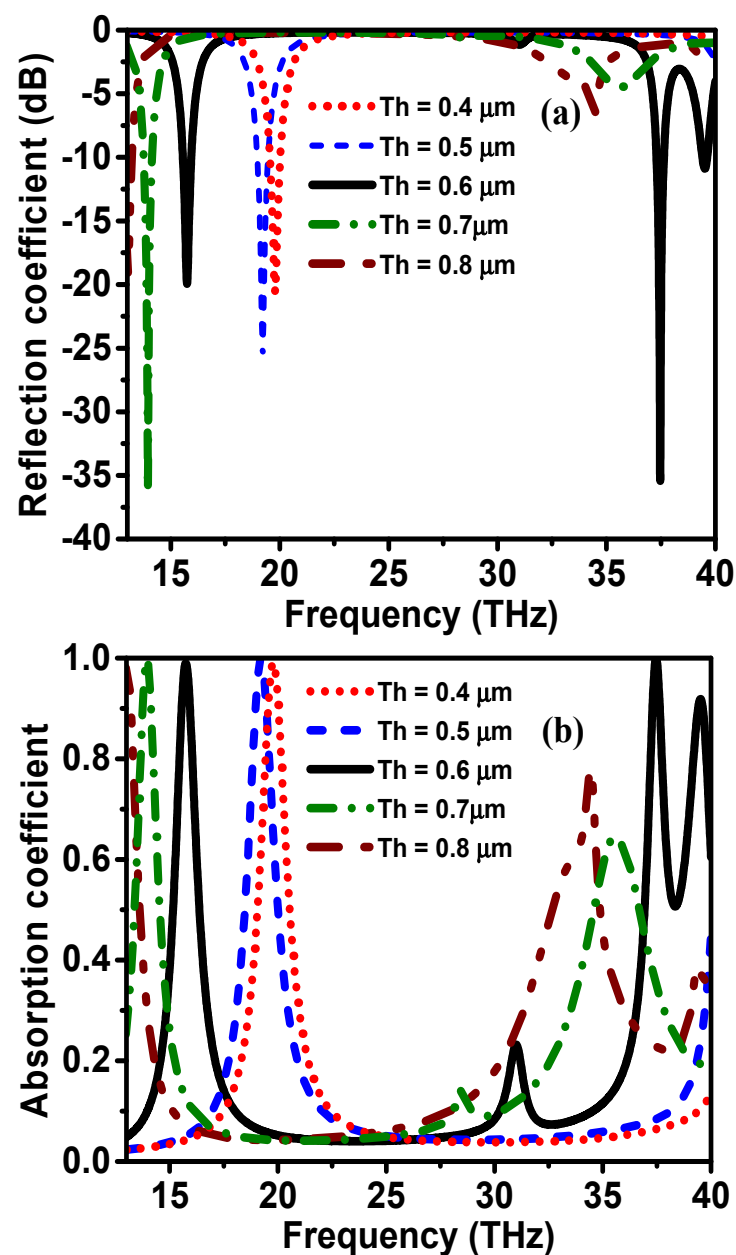


Figure 5. Effect of substrate thickness on the (a) reflection and (b) absorption coefficient of the proposed MTM.



#### 4.3. Effect of the Unit Cell Dimensions

Another important parameter in the design process is the unit cell dimension ( $L$ ). The unit cell size defines the area ( $L \times W$ ) of the ZnSe substrate on which the resonator is deposited. Since the proposed substrate is square ( $L = W$ ), the unit cell size can be expressed by  $L \times L$ . As such, changes in the unit cell size are directly related to changes in the radii ( $R$  and  $r$ ) of the resonator. When  $L$  changes, the size of the unit cell also changes. Five different unit cell sizes of  $6 \times 6 \text{ } (\mu\text{m})^2$ ,  $7 \times 7 \text{ } (\mu\text{m})^2$ ,  $8 \times 8 \text{ } (\mu\text{m})^2$ ,  $9 \times 9 \text{ } (\mu\text{m})^2$  and  $10 \times 10 \text{ } (\mu\text{m})^2$ —named size 1, size 2, size 3, size 4, and size 5, respectively—were considered. The absorption spectra for the different unit cell sizes are shown in Figure 6. The absorption spectra varied for different sizes. This could be mainly due to the effects of the wavelength, where each resonator operates at a particular frequency. Hence, the impact of the unit cell size on the absorption profile can be seen to significantly shift the absorption peaks at 37.48 and 39.55 THz, while there is not a significant shift in the absorption peak at 15.68 THz (see Figure 6). From this parametric study, an optimum condition was set such that the proposed MTM resonator achieved maximum absorption.

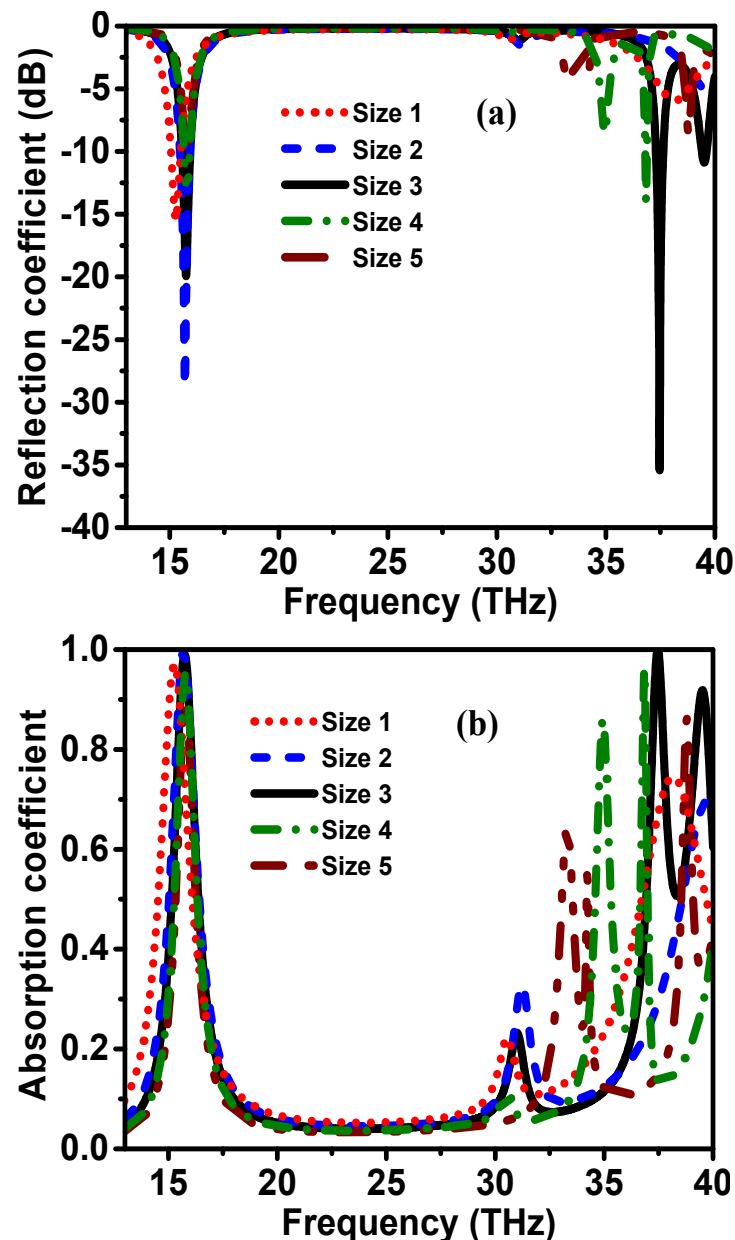


Figure 6. Effect of the unit size dimension on the (a) reflection and (b) absorption coefficient of the proposed MTM.

#### 4.4. Effect of Split Gap Variation

In this section, a parametric analysis was conducted to observe the effect of changing the split gap dimension. The split gap was changed from  $0.5\ \mu\text{m}$  in steps of  $0.5\ \mu\text{m}$ . An increase in the split gap dimension significantly changed the resonance peaks, as shown in Figure 7. This resonance shift could be attributed to changes in the capacitive effect on the resonator due to the split gap. For instance, each resonator layer corresponds to an RLC circuit—hence, when the capacitance of the resonator is changed, the resonance frequency also varies. The optimum operating parameter of the split gap was chosen as  $0.5\ \mu\text{m}$ .

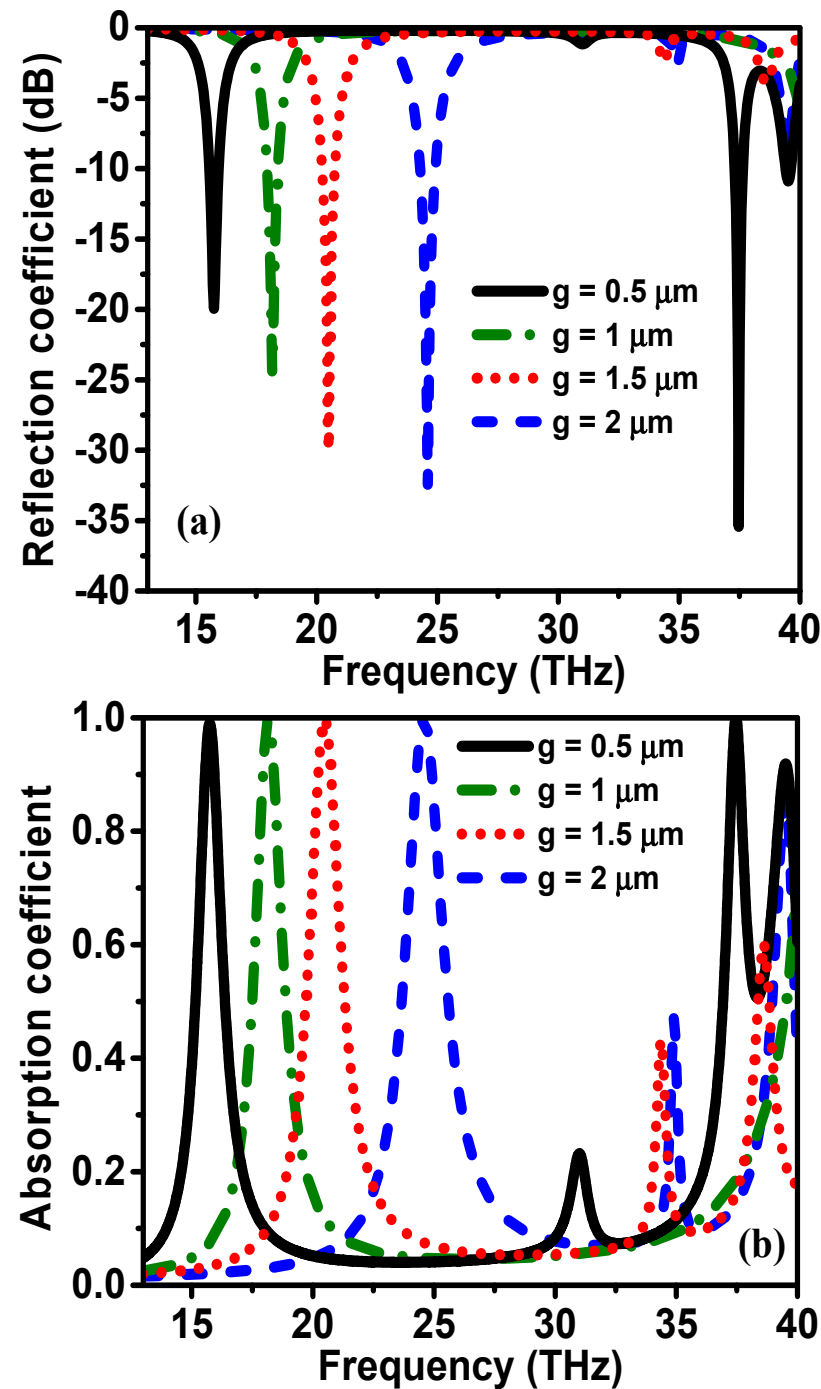


Figure 7. Effect of the split gap change on the (a) reflection and (b) absorption spectra of the proposed MTM.

#### 4.5. Effect of Substrate Type

Finally, the effects of the different substrate materials were investigated. Figure 8 shows the absorption spectra for the ZnSe, FR4, Rogers RT5870, and Arlon AD410 substrates; variations were caused by differences in the dielectric constant and loss tangent of the materials. The dielectric constants of these materials were 5.73, 4.3, 2.33, and 4.10, respectively, while their corresponding loss tangents are 1, 0.025, 0.0012, and 0.003, respectively. This analysis obtained the best absorption spectra with the ZnSe-based resonator, as shown in Figure 8. The thickness of the substrate was fixed at  $0.6\ \mu\text{m}$ . One can see that the FR4 and Arlon AD410 dielectric substrates created similar resonances, and the Rogers RT5870 could generate only one resonance peak. However, the proposed ZnSe Pro substrate produced three resonances. Thus, the ZnSe material was chosen as the substrate for the MTM design. It can be seen from Figure 8 that the peak at about 31 THz appeared when the substrate type was ZnSe. Therefore, this peak is mainly attributed to the ZnSe substrate in the frequency window of 10 to 40 THz. Consequently, any changes in the substrate thickness and substrate size (unit cell size) led to changes in the position and magnitude of the peak at 31 THz, as can be seen in Figures 5 and 6.

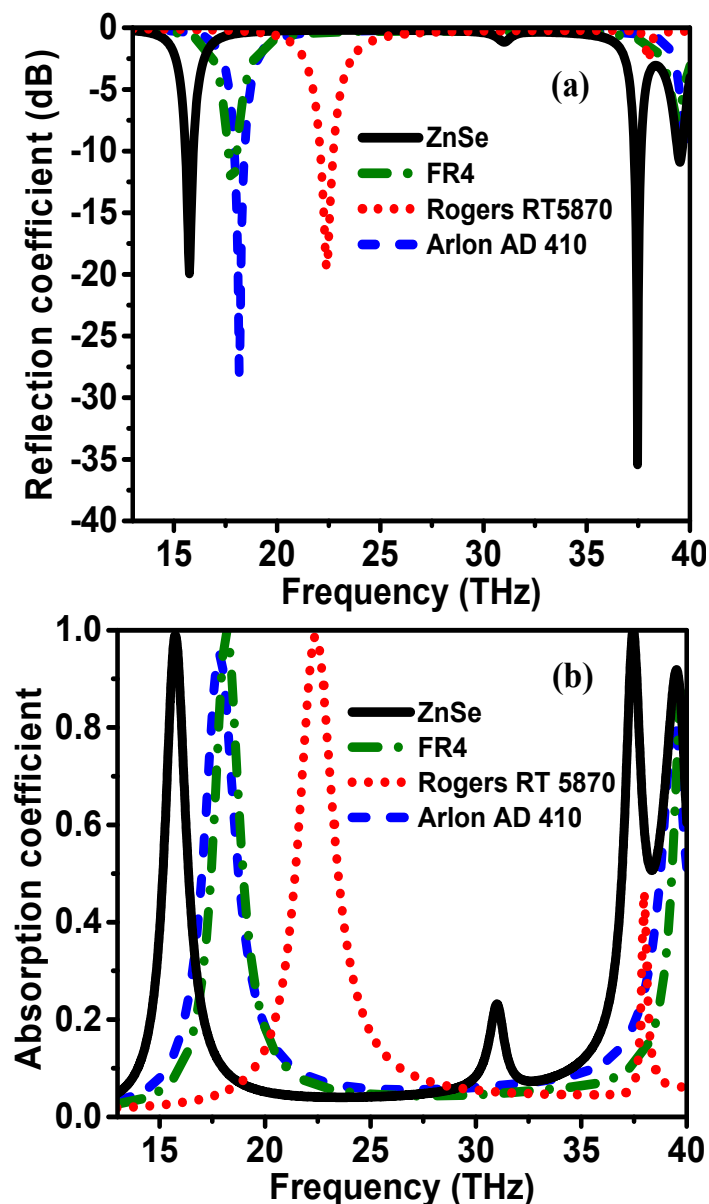
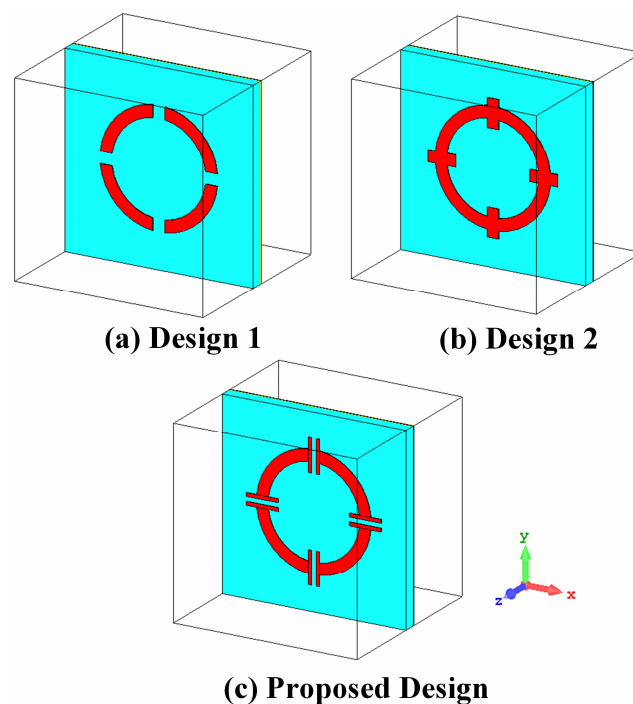


Figure 8. Frequency versus (a) S11 and (b) absorption curves for different substrate materials.

## 5. Selection of the Proposed Metamaterial Unit Cell

We designed and simulated two more designs to compare the proposed structure, as shown in Figure 9. Design 1 had split gaps only, so it did not have any patches in the splits nearby. Design 2 was composed of metallic patches placed at the split gaps of the ring resonators. The reflection and absorption spectra were simulated for the designs and given in Figure 9, while the obtained results are shown in Figure 10. It can be seen from Figure 10a,b that the multiband perfect absorptivity and reflection characteristics reached their optimum values. As design 2 did not have splits, it did not present a multiband absorptivity. Although design 1 was similar to the proposed structure, it did not provide multiband absorptivity in the given frequency band. Furthermore, the absorption peaks were not prominent. For these reasons, the proposed design was chosen, and its dimensions were optimized for the best performance and absorptivity, together with its insensitivity to the incident and polarization angles.



**Figure 9.** Simulation of the three different structures: (a) Design 1, (b) Design 2, and (c) Proposed design.

Figure 10 shows the reflection and absorption spectra obtained for design 1, design 2, and the proposed design in the frequency range from 13 to 40 THz. Changes in the resonance frequency were observed among the three designs, which can be related to the presence of capacitive variations in the equation  $f_0 = \frac{1}{2\pi\sqrt{LC}}$ . The first design comprised a conventional circular ring resonator, having four capacitive gaps. The results showed that design 1 could provide a single resonance frequency at 21 THz, as illustrated in Figure 10. The capacitive gaps were removed in the second design to present a unit cell with a basic circular ring. The overall capacitive effect in design 2 decreased dramatically due to the elimination of these gaps. Therefore, the resonance frequency increased (blue shifted) to 36.5 THz owing to the minimization of the capacitance part of the equation. However, four capacitive split gaps were again placed into the unit cell in the proposed design, as shown in Figure 9c. The difference between the proposed design and design 1 was due to the length of the parallel plates at the split gaps and the distance between them; these variations in the proposed design increased the capacitance of the unit cell. With increases in the capacitive effects of the proposed design, the resonance frequency decreased (redshifted) to 15.68 THz. Moreover, two different absorption peaks were obtained for the proposed design in these terahertz regimes.

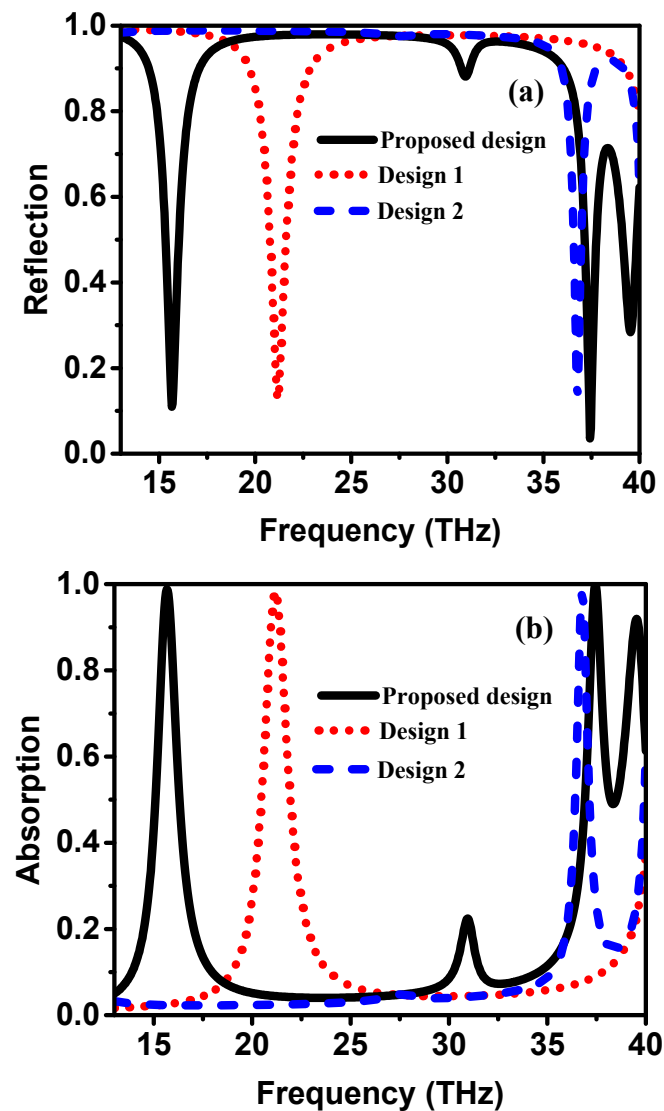
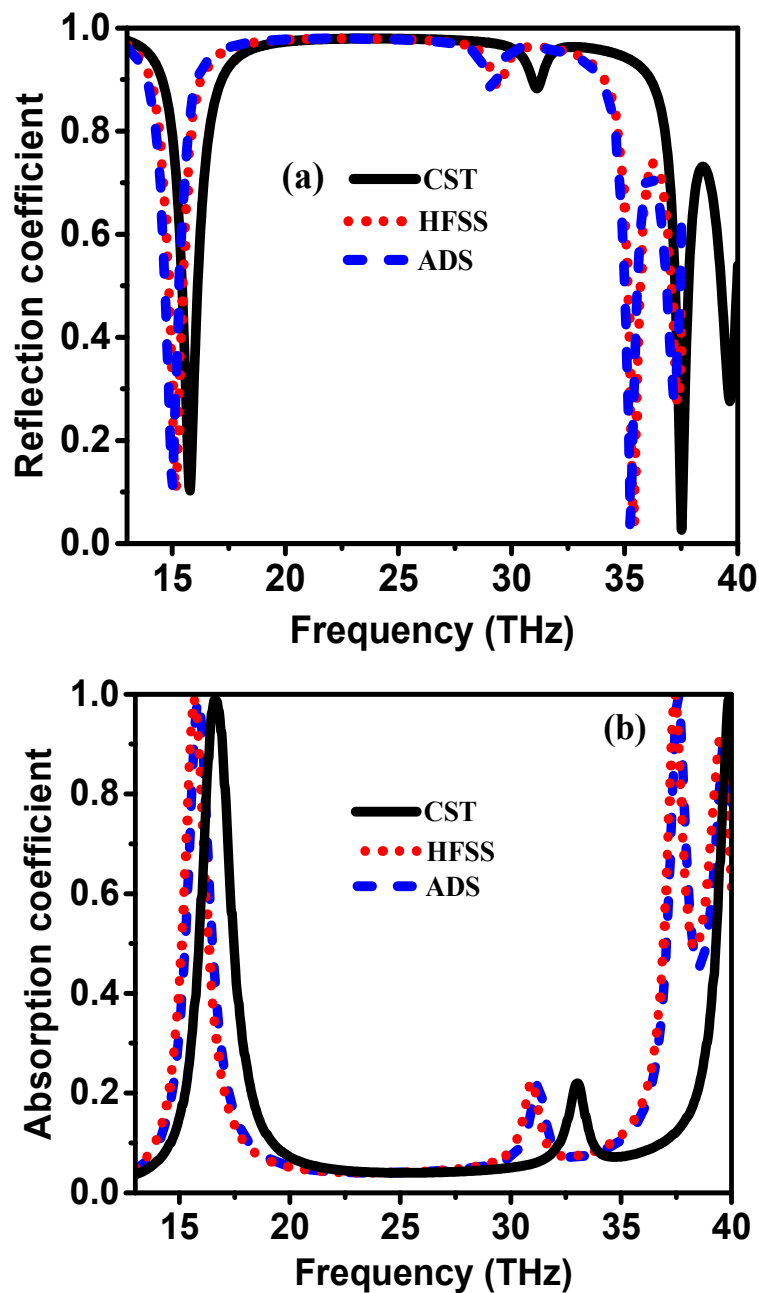


Figure 10. (a) Simulated Reflection spectra and (b) Absorption spectra of the three different structures.

## 6. Analysis of Different Software Simulations for the Proposed Design

The numerical studies of the proposed ultrathin, triple band, and perfect metamaterial absorber were also validated using three different simulation software—namely, High Frequency Simulation Software (HFSS), Advanced Design System (ADS), and Computer Simulation Technology (CST). In the ADS, 3D dielectric bricks or bond wire arcs can be simulated using the finite element method (FEM) or method of moments (MOM). HFSS has an efficient solver for radiation and scattering. The main solver of HFSS is FEM, while it also has MOM solution. CST is based on finite integration techniques (FIT) and finite difference time domains (FDTDs) for transient solutions; it also uses FEM and MOM for the frequency domain and as an integral equation solver. It was found from the simulation results that the reflection and absorption spectra had almost the same response, as shown in Figure 11. Specifically, the HFSS and ADS results were highly matched, as they were built on the same solution technique. Nevertheless, the CST result was slightly different from that of the HFSS and ADS, confirming the absorption behavior of the proposed structure.



**Figure 11.** Simulated results for the proposed design obtained by three different software (HFSS, CST and ADS) for (a) reflection coefficients and (b) absorption spectrum coefficients.

### 7. Surface Current, Electric Field, and Magnetic Field Analysis

Field distributions are important for understanding wave propagation and resonance modes [59]. Figure 12 shows the surface-current distribution across the resonator and the ground plane at the three characteristic resonance frequencies of 15.68, 37.48, and 39.55 THz. It can be seen from Figure 12a that at the resonance frequency of 15.68 THz, the current flow in the upper- and lower-half parts of the resonator were parallel, while they were anti-parallel to the current flow in the ground plane. This led to the formation of a weak electric field distribution across the ring resonator arms, but a relatively strong electric field across the horizontal splits (vertical capacitors)—as can be noticed in Figure 13a. Nevertheless, at the resonance frequency of 37.48 THz, the current distribution intensity was lower. However, the current flow in the resonator and the ground plane were parallel—especially around the ring resonator’s left- and right-half arms, as shown in Figure 12b. Consequently, the induced electric field got stronger, as

shown in Figure 13b. It is worth noting from Figure 12c that at the higher resonance frequency of 39.55 THz, the electric current flow around the horizontally loaded capacitors (vertical split) and the ground plane were aligned parallelly—thereby enhancing the overall electric field distribution around these two capacitors, as shown in Figure 13c.

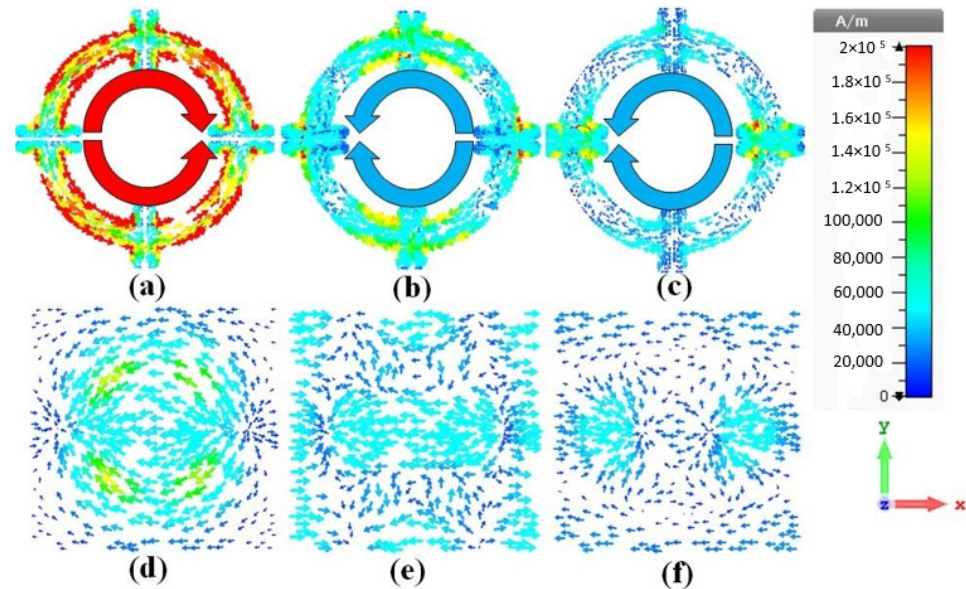


**Figure 12.** Simulated surface current distribution at the resonator (a) 15.68 THz, (b) 37.48 THz, (c) 39.55 THz, (d,e), and (f) at the ground plane for the same frequencies for the triple-band MPA, respectively.

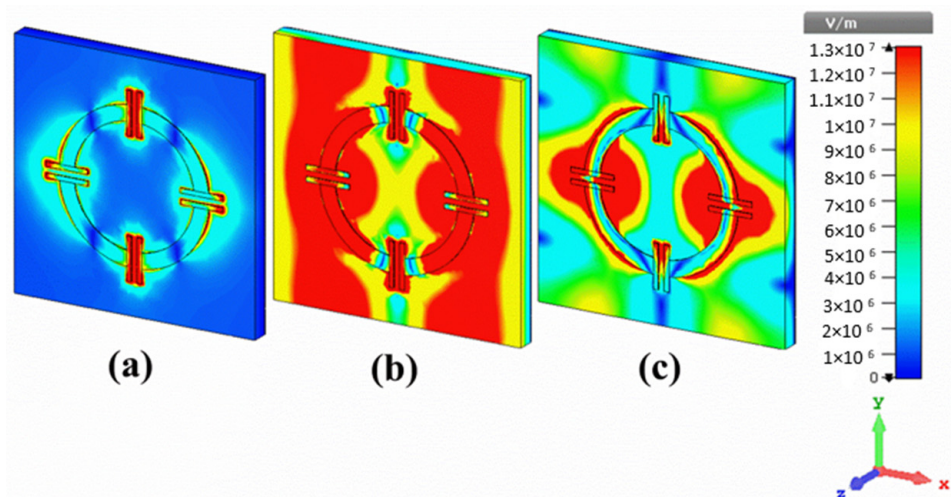


**Figure 13.** Electric field distribution at three different resonance peaks (a) 15.68 THz (b) 37.48 THz and (c) 39.55 THz for the proposed design.

Ultimately, the consequence of the current flow and electric field distributions play an important role in shaping the magnetic properties of the MTM resonator. Therefore, from Figure 14a, one can observe that the strongest magnetic field distribution was achieved at the resonance frequency of 15.68 THz, where the current in the resonator and ground plane were flowing in the opposite directions. The minimal level of occurrence of the intense magnetic field was because of the induced magnetic field induced by the MTM; there was not any magnetic opposition against the externally applied magnetic field in the y-axis direction. Noteworthy, it can be concluded from Figure 14b,c that when the resonance frequency increased, the magnetic field distribution around the left- and right-arms of the ring resonator significantly decreased; this can be ascribed to the relatively high electric

field at these positions (see Figure 13b,c). Therefore, the induced magnetic field by the MTM due to the parallel current flow led to the formation of an induced magnetic field which acted against the external magnetic field, according to Lenz's law.

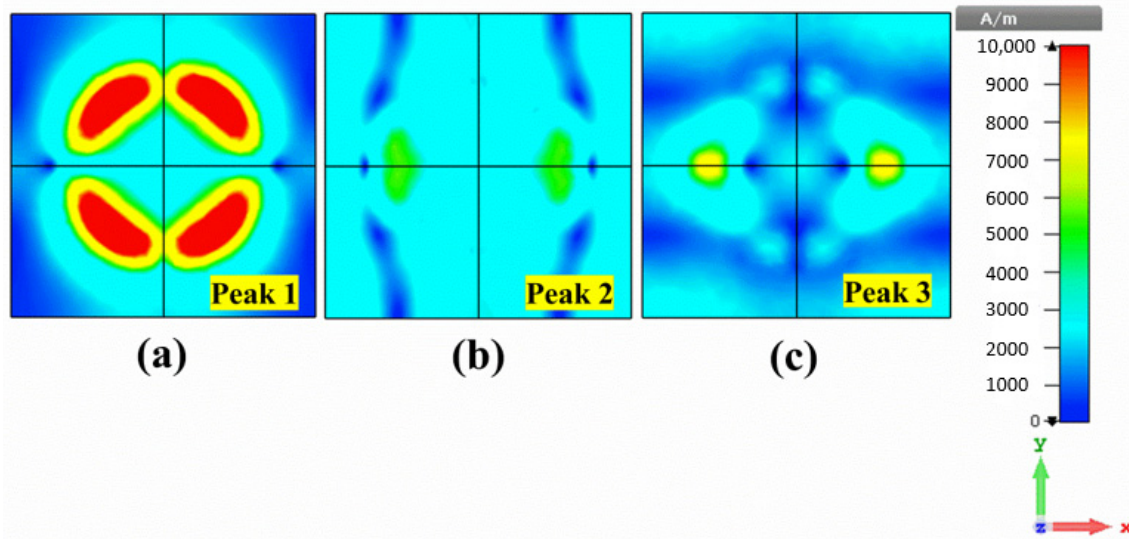


**Figure 14.** Magnetic field distribution at three different resonance peaks (a) 15.68 THz (b) 37.48 THz and (c) 39.55 THz for the triple band metamaterial perfect absorber.

Tables 2 and 3 show the comparison of the overall performance of the proposed MTM structure with that of other works reported in the literature. Comparatively, it can be seen from Table 2 that, based on the shape of the MTM unit cell, frequency operation, dimension unit cell, thickness of the used substrate, absorptivity, and peak numbers, the proposed design has a smaller unit cell of  $8 \times 8 \mu\text{m}^2$  and possesses an ultra-thin property of  $0.6 \mu\text{m}$ . Hence, in addition to the reduction in the device profile, the absorptivity is high and its absorption characteristics are independent of the polarization angle compared to those of other designs reported in the literature.

**Table 2.** Parametric analysis of the proposed and existing metamaterials.

Ref.	Shape of the MTM Unit Cell	Frequency Operating THz	Unit Cell Size ( $\mu\text{m}^2$ )	Substrate Thickness ( $\mu\text{m}$ )	Absorptivity (%)	Peak Numbers
[12]	Multiple metallic resonators	2–5	$36 \times 36$	2	100–97	Dual
[13]	cross metal array resonator	12–28	$4 \times 4$	1.5	99	Single
[14]	two nested metallic circular ring resonators	0–4.5	$80 \times 80$	18	99.96–98.92–99.83–99.35 and 99	Five
[15]	Gold resonator	4–8	$43.8 \times 43.8$	8.1	99.3–99.2–99.4–95.2 and 98.1	Five
[16]	Periodic cross-shaped grooves	0–3.5	$50 \times 50$	45	97.80–95.8	Dual
[22]	metallic cross-cave-patch (CCP)	0.4–2.2	$90 \times 90$	8	98.0, 99.6, 95.2, 97.9, 96.7 and 99.9	Six
[23]	metal square ring and four metallic cylinders	1.2–2.5	$60 \times 60$	7	99.9	Single
[43]	four-fold meander wire	1–3	$55 \times 50$	15	93–100	Dual
[44]	Au Reflector	2–8	$30 \times 35$	5	99–99	Dual
[45]	split ring dish resonator	1.925–6.3	$24 \times 24$	1.2	100–99–100	Single/Dual
[46]	Au rectangular strips	0–4.05	$60 \times 60$	2	100–99–99	Triple
[47]	graphene based meshed square patch FSS	0–4	$42 \times 42$	22	99–97	Dual
[52]	Single metallic resonator	15–35	$9.5 \times 9.5$	0.6	98.44–99.28	Dual
This Work	Single copper resonator	13–40	$8 \times 8$	0.6	99–99.85 and 92.25	Triple



**Table 3.** Comparison between the suggested structure and existing MTM absorber.

Ref.	Techniques Used	Central Frequency	Absorption	Polarization	Angles	Year Published
[12]	Al/TiO <sub>2</sub> /Al	3.5	>90%	TE and TM	0–90	2020
[13]	Metal layer/Dielectric layer/Metal layer	20	>90%	-	0–50	2020
[14]	Copper/Polyimide/Silicon	2.25	>90%	-	0–90	2018
[15]	Au/Graphene/SiO <sub>2</sub> /Au	5.51	>90%	TE and TM	0–90	2020
[16]	Gold/SiO <sub>2</sub> /Graphene/SiO <sub>2</sub>	0.94	>90%	-	-	2019
[22]	Gold/InSb/gold	1.3	>90%	-	-	2019
[23]	Gold/InSb/gold	1.85	>90%	TE and TM	0–90	2020
[43]	Gold/PDMS/Gold	2	>90%	TE and TM	0–90	2018
[44]	Au/SiO <sub>2</sub> /Au	5	>90%	-	-	2019
[45]	Gold/SiO <sub>2</sub> /Gold	4.375	>90%	TE	0–60	2018
[46]	Au/dielectric slab/Au	2.25	>90%	-	-	2019
[47]	Graphene FSS/polyimide layer/perfect electric conductor (PEC)	2	>90%	TE	0–60	2020
[48]	Copper/ZnSe/Copper	25	>90%	TE and TM	0–60	2021
This Work	Metal/ZnSe/Metal	27	>90%	TE or TM	0–90	2022

## 8. Conclusions

In this work, we successfully designed and analyzed a low-profile metamaterial-based perfect absorber in the THz frequency range. The proposed design consists of a symmetric four-capacitance loaded complementary circular split ring resonator on the top of an ultra-thin ZnSe substrate. The back side of the structure is covered by a metal plate to prevent transmission, and a triple-band MTM perfect absorber was obtained. It was found that with the help of parametric studies in the optimization of the proposed structure, three high absorptive peaks with nearly perfect absorption were obtained at the resonance frequencies of 15.68, 37.48, and 39.55 THz. Furthermore, the absorber was insensitive to the polarization angle and incident wave angle from 0° to 90°. It was concluded that the overall performance of the proposed MTM structure is superior compared to that of other reported structures.

**Author Contributions:** Conceptualization, Y.I.A., F.F.M. and M.K.; methodology, Y.I.A. and B.A.; software, Y.I.A. and F.Ö.A.; validation, O.A. and H.N.A.; investigation, Y.I.A. and J.D.; resources, Y.I.A., M.B., M.T.; data curation, Y.I.A.; writing—original draft preparation, Y.I.A., M.K., F.F.M. and J.D.; supervision, J.D. and B.A.; project administration, B.A.; formal analysis: J.D.; funding acquisition: B.A.; visualization: Y.I.A. and M.K.; writing—review and editing: Y.I.A., O.A. and H.N.A.; figures and tables: M.B. and M.T. All authors have read and agreed to the published version of the manuscript.

**Funding:** There is no funding available for this.

**Institutional Review Board Statement:** Not applicable.

**Informed Consent Statement:** Not applicable.

**Data Availability Statement:** Not applicable.

**Conflicts of Interest:** The authors declare no conflict of interest.

## References

- Abdulkarim, Y.I.; Deng, L.; Yang, J.-L.; Çolak, Ş.; Karaaslan, M.; Huang, S.-X.; He, L.-H.; Luo, H. Tunable left-hand characteristics in multi-nested square-split-ring enabled metamaterials. *J. Cent. South Univ.* **2020**, *27*, 1235–1246. [\[CrossRef\]](#)
- Wang, W.; Yan, F.; Tan, S.; Zhou, H.; Hou, Y. Ultrasensitive terahertz metamaterial sensor based on vertical split ring resonators. *Photonics Res.* **2017**, *5*, 571–577. [\[CrossRef\]](#)
- Ekmekci, E.; Turhan-Sayan, G. Multi-functional metamaterial sensor based on a broad-side coupled SRR topology with a multi-layer substrate. *Appl. Phys. A* **2013**, *110*, 189–197. [\[CrossRef\]](#)
- Dhama, R.; Yan, B.; Palego, C.; Wang, Z. Super-Resolution Imaging by Dielectric Super lenses: TiO<sub>2</sub> Metamaterial Superlens versus BaTiO<sub>3</sub> Super lens. *Photonics* **2021**, *8*, 222. [\[CrossRef\]](#)
- Haxha, S.; AbdelMalek, F.; Ouerghi, F.; Charlton, M.D.B.; Aggoun, A.; Fang, X.J.S.R. Metamaterial super lenses operating at visible wavelength for imaging applications. *Sci. Rep.* **2018**, *8*, 16119. [\[CrossRef\]](#)
- Manjappa, M.; Pitchappa, P.; Wang, N.; Lee, C.; Singh, R. Active control of resonant cloaking in a terahertz MEMS metamaterial. *Adv. Opt. Mater.* **2018**, *6*, 1800141. [\[CrossRef\]](#)

7. Islam, S.S.; Hasan, M.M.; Faruque, M.R.I. A new metamaterial-based wideband rectangular invisibility cloak. *Appl. Phys. A* **2018**, *124*, 160. [[CrossRef](#)]
8. Imani, M.F.; Gollub, J.N.; Yurduseven, O.; Diebold, A.V.; Boyarsky, M.; Fromenteze, T.; Pulido-Mancera, L.; Sleasman, T.; Smith, D.R. Review of Metasurface Antennas for Computational Microwave Imaging. *IEEE Trans. Antennas Propag.* **2020**, *68*, 1860–1875. [[CrossRef](#)]
9. Abdulkarim, Y.I.; Awl, H.N.; Muhammadsharif, F.F.; Karaaslan, M.; Mahmud, R.H.; Hasan, S.O.; Işık, Ö.; Luo, H.; Huang, S. A Low-Profile Antenna Based on Single-Layer Metasurface for Ku-Band Applications. *Int. J. Antennas Propag.* **2020**, *2020*, 8813951. [[CrossRef](#)]
10. Alkurt, F.O.; Altintas, O.; Atci, A.; Bakir, M.; Unal, E.; Akgol, O.; Sabah, C. Antenna-based microwave absorber for imaging in the frequencies of 1.8, 2.45, and 5.8 GHz. *Opt. Eng.* **2018**, *57*, 113102. [[CrossRef](#)]
11. Abdulkarim, Y.I.; Deng, L.; Altıntaş, O.; Ünal, E.; Karaaslan, M. Metamaterial absorber sensor design by incorporating swastika shaped resonator to determination of the liquid chemicals depending on electrical characteristics. *Phys. E Low-Dimens. Syst. Nanostruct.* **2019**, *114*, 113593. [[CrossRef](#)]
12. Daniel, S.; Bawuah, P. Right-Angle Shaped Elements as Dual-Band Metamaterial Absorber in Terahertz. *Photonic Sens.* **2019**, *10*, 233–241. [[CrossRef](#)]
13. Zhong, M. Design and measurement of a narrow band metamaterial absorber in terahertz range. *Opt. Mater.* **2020**, *100*, 109712. [[CrossRef](#)]
14. Meng, T.; Hu, D.; Zhu, Q. Design of a five-band terahertz perfect metamaterial absorber using two resonators. *Opt. Commun.* **2018**, *415*, 151–155. [[CrossRef](#)]
15. Jain, P.; Bansal, S.; Prakash, K.; Sardana, N.; Gupta, N.; Kumar, S.; Singh, A.K. Graphene-based tunable multi-band metamaterial polarization-insensitive absorber for terahertz applications. *J. Mater. Sci. Mater. Electron.* **2020**, *31*, 11878–11886. [[CrossRef](#)]
16. Qi, L.; Liu, C.; Mohsin, S. Ali Shah A broad dual-band switchable graphene-based terahertz metamaterial absorber. *Carbon* **2019**, *153*, 179–188. [[CrossRef](#)]
17. Abdulkarim, Y.I.; Muhammadsharif, F.F.; Bakır, M.; Awl, H.N.; Karaaslan, M.; Deng, L.; Huang, S. Hypersensitized Metamaterials Based on a Corona-Shaped Resonator for Efficient Detection of Glucose. *Appl. Sci.* **2021**, *11*, 103. [[CrossRef](#)]
18. Abdulkarim, Y.I.; Deng, L.; Luo, H.; Huang, S.; Karaaslan, M.; Altıntaş, O.; Bakır, M.; Muhammadsharif, F.F.; Awl, H.N.; Sabah, C.; et al. Design and study of a metamaterial based sensor for the application of liquid chemicals detection. *J. Mater. Res. Technol.* **2020**, *9*, 10291–10304. [[CrossRef](#)]
19. Abdulkarim, Y.I.; Deng, L.; Karaaslan, M.; Altıntaş, O.; Awl, H.N.; Muhammadsharif, F.F.; Liao, C.; Unal, E.; Luo, H. Novel metamaterials-based hypersensitized liquid sensor integrating omega-shaped resonator with microstrip transmission line. *Sensors* **2020**, *20*, 943. [[CrossRef](#)]
20. Abdulkarim, Y.I.; Deng, L.; Muhrram, K.; Eunal, U. Determination of the liquid chemicals depending on the electrical characteristics by using metamaterial absorber based sensor. *Chem. Phys. Lett.* **2019**, *732*, 136655. [[CrossRef](#)]
21. Aslinezhad, M. High sensitivity refractive index and temperature sensor based on semiconductor metamaterial perfect absorber in the terahertz band. *Opt. Commun.* **2020**, *463*, 125411. [[CrossRef](#)]
22. Zou, H.; Cheng, Y. Design of a six-band terahertz metamaterial absorber for temperature sensing application. *Opt. Mater.* **2019**, *88*, 674–679. [[CrossRef](#)]
23. Zou, H.; Cheng, Y. A thermally tunable terahertz three-dimensional perfect metamaterial absorber for temperature sensing application. *Mod. Phys. Lett. B* **2020**, *34*, 2050207. [[CrossRef](#)]
24. Xu, C.; Qu, S.; Pang, Y.; Wang, J.; Yan, M.; Zhang, J.; Wang, Z.; Wang, W. Metamaterial absorber for frequency selective thermal radiation. *Infrared Phys. Technol.* **2018**, *88*, 133–138. [[CrossRef](#)]
25. He, Y.; Wu, Q.; Yan, S. Multi-Band Terahertz Absorber at 0.1–1 THz Frequency Based on Ultra-Thin Metamaterial. *Plasmonics* **2019**, *14*, 1303–1310. [[CrossRef](#)]
26. Jianjun, L.; Lanlan, F. Development of a tunable terahertz absorber based on temperature control. *Microw. Opt. Technol. Lett.* **2020**, *62*, 1681–1685. [[CrossRef](#)]
27. Ito, K.; Watari, T.; Nishikawa, K.; Yoshimoto, H.; Iizuka, H. Inverting the thermal radiative contrast of vanadium dioxide by metasurfaces based on localized gap-plasmons. *APL Photonics* **2018**, *3*, 086101. [[CrossRef](#)]
28. Zhang, X.; Zhang, Z.-G.; Wang, Q.; Zhu, S.-N.; Liu, H. Controlling thermal emission by parity-symmetric fano resonance of optical absorbers in metasurfaces. *ACS Photonics* **2019**, *6*, 2671–2676. [[CrossRef](#)]
29. Ustunsoy, M.P.; Sabah, C. Dual-band high-frequency metamaterial absorber based on patch resonator for solar cell applications and its enhancement with graphene layers. *J. Alloys Compd.* **2016**, *687*, 514–520. [[CrossRef](#)]
30. Hoque, A.; Islam, M.T. Numerical analysis of single negative broadband metamaterial absorber based on tri thin layer material in visible spectrum for solar cell energy harvesting. *Plasmonics* **2020**, *15*, 1061–1069. [[CrossRef](#)]
31. Bagmanci, M.; Karaaslan, M.; Unal, E.; Akgol, O.; Bakır, M.; Sabah, C. Solar energy harvesting with ultra-broadband metamaterial absorber. *Int. J. Mod. Phys. B* **2019**, *33*, 1950056. [[CrossRef](#)]
32. Li, W.; Fan, S. Nano photonic control of thermal radiation for energy applications. *Opt. Express* **2018**, *26*, 15995–16021. [[CrossRef](#)] [[PubMed](#)]
33. Wang, W.; Zhao, Z.; Zou, Q.; Hong, B.; Zhang, W.; Wang, G.P. Self-adaptive radiative cooling and solar heating based on a compound metasurface. *J. Mater. Chem. C* **2020**, *8*, 3192–3199. [[CrossRef](#)]

34. Smith, E.M.; Chen, J.; Hendrickson, J.R.; Cleary, J.W.; Dass, C.; Reed, A.N.; Vangala, S.; Guo, J. Epsilon-near-zero thin-film metamaterials for wideband near-perfect light absorption. *Opt. Mater. Express* **2020**, *10*, 2439–2446. [[CrossRef](#)]
35. Cheng, Y.; Zhao, H.; Li, C. Broadband tunable terahertz metasurface absorber based on complementary-wheel-shaped graphene. *Opt. Mater.* **2020**, *109*, 110369. [[CrossRef](#)]
36. Chen, F.; Cheng, Y.; Luo, H. A Broadband Tunable Terahertz Metamaterial Absorber Based on Single-Layer Complementary Gammadion-Shaped Graphene. *Materials* **2020**, *13*, 860. [[CrossRef](#)]
37. Li, W.; Cheng, Y. Dual-band tunable terahertz perfect metamaterial absorber based on strontiumtitanate (STO) resonator structure. *Opt. Commun.* **2020**, *462*, 125265. [[CrossRef](#)]
38. Zhang, Y.; Wu, P.; Zhou, Z.; Chen, X.; Yi, Z.; Zhu, J.; Jile, H. Study on temperature adjustable terahertz metamaterial absorber based on vanadium dioxide. *IEEE Access* **2020**, *8*, 85154–85161. [[CrossRef](#)]
39. Wang, B.X.; He, Y.; Lou, P.; Xing, W. Design of a dual-band terahertz metamaterial absorber using two identical square patches for sensing application. *Nanoscale Adv.* **2020**, *2*, 763–769. [[CrossRef](#)]
40. Liu, H.; Wang, Z.H.; Li, L.; Fan, Y.X.; Tao, Z.Y. Vanadium dioxide-assisted broadband tunable terahertz metamaterial absorber. *Sci. Rep.* **2019**, *9*, 5751. [[CrossRef](#)]
41. Huang, M.L.; Cheng, Y.Z.; Cheng, Z.Z.; Chen, H.R.; Mao, X.S.; Gong, R.Z. Design of a broadband tunable terahertz metamaterial absorber based on complementary structural graphene. *Materials* **2018**, *11*, 540. [[CrossRef](#)]
42. Wang, R.; Li, L.; Liu, J.; Yan, F.; Tian, F.; Tian, H.; Sun, W. Triple-band tunable perfect terahertz metamaterial absorber with liquid crystal. *Opt. Express* **2017**, *25*, 32280–32289. [[CrossRef](#)]
43. Cheng, Y.; Zou, H.; Yang, J.; Mao, X.; Gong, R. Dual and broadband terahertz metamaterial absorber based on a compact resonator structure. *Opt. Mater. Express* **2018**, *8*, 3104. [[CrossRef](#)]
44. Zhang, Y.; Cen, C.; Liang, C.; Yi, Z.; Chen, X.; Li, M.; Zhou, Z.; Tang, Y.; Yi, Y.; Zhang, G. Dual-band switchable terahertz metamaterial absorber based on metal nanostructure. *Results Phys.* **2019**, *14*, 102422. [[CrossRef](#)]
45. Jain, P.; Singh, A.K.; Pandey, J.K.; Bansal, S.; Gupta, N.; Singh, A.K.; Kumar, S.; Sardana, N. Ultra-thin and Dual Band Metamaterial Absorber for Terahertz Applications. In Proceedings of the 6th Edition of International Conference on Wireless Networks & Embedded Systems (WECON), Rajpura, India, 16–17 November 2018; p. 8951284. [[CrossRef](#)]
46. Wang, B.-X.; Tang, C.; Niu, Q.; He, Y.; Chen, T. Design of Narrow Discrete Distances of Dual-/Triple-Band Terahertz Metamaterial Absorbers. *Nanoscale Res. Lett.* **2019**, *16*, 64. [[CrossRef](#)]
47. Mishra, R.; Panwar, R. Investigation of graphene fractal frequency selective surface loaded terahertz absorber. *Opt. Quantum Electron.* **2020**, *52*, 317. [[CrossRef](#)]
48. Zamzam, P.; Rezaei, P.; Khatami, S.A. Quad-band polarization-insensitive metamaterial perfect absorber based on bilayer graphene metasurface. *Phys. E Low-Dimens. Syst. Nanostruct.* **2021**, *128*, 114621. [[CrossRef](#)]
49. Sayeed, M.A.; Rouf, H.K. Fabrication and Characterization of Zinc Selenide (ZnSe) Thin Film in Solar Cell Applications. In Proceedings of the International Conference on Innovations in Science, Engineering and Technology, Chittagong, Bangladesh, 27–28 October 2018. [[CrossRef](#)]
50. Choudhari, U.; Jagtap, S. Hydrothermally Synthesized ZnSe Nanoparticles for Relative Humidity Sensing Application. *J. Electron. Mater.* **2020**, *49*, 5903–5916. [[CrossRef](#)]
51. Zhenhong, W.; Feng, L.; Jia, G.; Chunyang, M.; Yufeng, S.; Zhenwu, H.; Jun, L.; Yupeng, Z.; Delong, L.; Han, Z. Facile Synthesis of 2D Tin Selenide for Near- and Mid-Infrared Ultrafast Photonics Applications. *Adv. Opt. Mater.* **2020**, *8*, 1902183. [[CrossRef](#)]
52. Cheng, Y.; Gong, R.; Cheng, Z. A photo excited broadband switchable metamaterial absorber with polarization-insensitive and wide-angle absorption for terahertz waves. *Opt. Commun.* **2016**, *36*, 41. [[CrossRef](#)]
53. Cheng, Y.Z.; Huang, M.L.; Chen, H.R.; Guo, Z.Z.; Mao, X.S.; Gong, R.Z. Ultrathin six-band polarization-insensitive perfect metamaterial absorber based on a cross-cave patch resonator for terahertz waves. *Materials* **2017**, *10*, 591. [[CrossRef](#)]
54. Abdulkarim, I.Y.; Fatih, O.A.; Halgurd, N.A.; Fahmi, F.F.; Mehmet, B.; Sekip, D.; Muharrem, K.; Heng, L. An ultrathin and dual band metamaterial perfect absorber based on ZnSe for the polarization-independent in terahertz range. *Results Phys.* **2021**, *26*, 104344. [[CrossRef](#)]
55. Chen, H.-T. Interference theory of metamaterial perfect absorbers. *Opt. Express* **2012**, *20*, 7165–7172. [[CrossRef](#)]
56. Cheng, Y.; Nie, Y.; Gong, R. A polarization-insensitive and omnidirectional broadband terahertz metamaterial absorber based on coplanar multi-squares films. *Opt. Laser Technol.* **2013**, *48*, 415–421. [[CrossRef](#)]
57. Abdulkarim, I.Y.; Meiyu, X.; Halgurd, N.A.; Fahmi, F.F.; Lang, T.; Salah, R.S.; Fatih, O.A.; Mehmet, B.; Muharrem, K.; Jiang, D. Simulation and lithographic fabrication of a triple band terahertz metamaterial absorber coated on flexible polyethylene terephthalate substrate. *Opt. Mater. Express* **2022**, *12*, 338–359. [[CrossRef](#)]
58. Hema, O.A.; Al-Hindawi, A.M.; Abdulkarim, Y.I.; Nugoolcharoenlap, E.; Tippo, T.; Alkurt, F.Ö.; Altıntas, O.; Karaaslan, M. Simulated and experimental studies of a multi-band symmetric metamaterial absorber with polarization independence for radar applications. *Chin. Phys. B* **2022**, *31*, 058401. [[CrossRef](#)]
59. Tatjana, G.; Eldlio, M.; Cada, M.; Pistora, J. Analytic solution to field distribution in two-dimensional inhomogeneous waveguides. *J. Electromagn. Waves Appl.* **2015**, *29*, 1068–1081.